

Cite this: *Chem. Sci.*, 2024, 15, 19000

All publication charges for this article have been paid for by the Royal Society of Chemistry

Pyrazinoquinoxaline derivatives for flexible electronic devices: effect of the mechanical properties of the crystals on device durability†

Jasmine Bezboruah,^a Kanha Ram Khator,^{‡b} Sayantan Gayen,^{‡a} Devendra Mayurdhwaj Sanke,^{id a} Biplab Mahapatra,^b Anshuman Sahoo,^b Amlandeep Nayak,^b C. Malla Reddy,^{*ac} Satyaprasad P. Senanayak^{*bd} and Sanjio S. Zade^{id *a}

Understanding the interplay between the molecular structure and material properties of emerging p-type organic semiconductors marks a significant stride in the advancement of molecular electronics. Among the array of promising materials, mechanically flexible single crystals of π -conjugated molecules stand out due to their potential for cutting-edge applications in organic electronics. Notably, derivatives of pyrazinoquinoxaline (PQ) are recognized as versatile building blocks for constructing π -conjugated systems, showcasing good semiconductor performance in organic field-effect transistors (OFETs). In this study, we present an exploration into the p-type charge transport and mechanical characteristics of two newly synthesized PQ derivatives: 5,10-diphenyl-2,3,7,8-tetra(thiophen-2-yl)pyrazino[2,3-g]quinoxaline (DPTTQ) and 2,3,5,7,8,10-hexa(thiophen-2-yl)pyrazino[2,3-g]quinoxaline (HTPQ). HTPQ crystals exhibit flexural behaviour under applied stress, effortlessly returning to their initial configuration upon relaxation. Conversely, two polymorphic forms of DPTTQ crystals display brittle fracture when subjected to a similar stress. Specifically, DPTTQ molecules adopt a β -sheet packing, while HTPQ presents a γ -packing with a corrugated arrangement. Field-effect charge transport measurements reveal p-type charge transport in both DPTTQ and HTPQ, with HTPQ showcasing hole mobility up to $0.01 \text{ cm}^2 \text{ V}^{-1} \text{ s}^{-1}$, while DPTTQ exhibits mobility that is at least one order of magnitude lower. This variance in the field effect mobility can be directly correlated to the difference in crystal packing, highlighting a clear structure–property correlation. Moreover, taking advantage of the flexural nature of the HTPQ crystals, we fabricated durable electronic devices, which retain their conductivity for over 60 cycles of strain, indicating the efficacy of our chemical design in demonstrating high-performance flexible devices. These findings underscore the promise of semiconducting organics with γ -packing for achieving both better mobility and elasticity for integration into organic electronic devices.

Received 24th June 2024
Accepted 14th October 2024

DOI: 10.1039/d4sc04157g

rsc.li/chemical-science

Introduction

Organic semiconducting materials, distinguished by their distinctive advantages of room temperature processing,

tunability, and cost efficiency, have garnered significant interest in the realms of organic field-effect transistors (OFETs),^{1–3} organic light-emitting diodes (OLEDs),⁴ organic photovoltaics (OPVs),⁵ and sensors.⁶ Among these, OFETs have substantial commercial applicability in next-generation electronic devices.^{7–9} Flexible devices,^{10–12} possessing notable benefits like thinness, lightweight, foldability, and stretchability, show great potential for the future of electronics. This includes wearable smart electronic appliances such as e-skin, artificial intelligence, and robotics, indicating an upcoming revolution in human lifestyles.¹³ Over the past two decades, significant advancements have been made in high-performance flexible OFETs, and their utilization in flexible electronics has seen notable success.^{14,15}

Acenes are polycyclic aromatic compounds comprising linearly fused benzene rings.¹⁶ They have received a lot of interest in the field of materials science in recent decades due to their tuneable absorption, emission, and charge transfer

^aDepartment of Chemical Sciences and Centre for Advanced Functional Materials, Indian Institute of Science Education and Research (IISER) Kolkata, Mohanpur, 741246, Nadia, West Bengal, India. E-mail: cmreddy@chy.iith.ac.in; sanjiozade@iiserkol.ac.in

^bNanoelectronics and Device Physics Lab, National Institute of Science Education and Research, School of Physical Sciences, OCC of HBNI, Jatni, 752050, India. E-mail: satyaprasad@niser.ac.in

^cDepartment of Chemistry, Indian Institute of Technology Hyderabad, Kandi, Sangareddy, Telangana 502284, India

^dCenter for Interdisciplinary Sciences (CIS), NISER, An OCC of Homi Bhabha National Institute (HBNI), Jatni 752050, Odisha, India

† Electronic supplementary information (ESI) available. CCDC 2254836 and 2255405. For ESI and crystallographic data in CIF or other electronic format see DOI: <https://doi.org/10.1039/d4sc04157g>

‡ Contributed equally.

properties.^{17,18} The introduction of nitrogen atoms into the acene framework is regarded as a viable method of generating semiconducting materials with a variety of uses in electronic devices.¹⁹ Acenes with one or more C–H units replaced by pyridine-type nitrogen atoms are known as azaacenes or N-heteroacenes.²⁰ Azaacenes and their derivatives have a wide range of uses in OFETs.²¹

N-heteroarenes exhibit good field-effect mobilities, have environmental stability, and have sufficient solubility in common organic solvents.⁹ The position and the number of nitrogen atoms in the acene framework determine the solubility, stability, and electronic properties of N-heteroarenes.²² As a result, it is worthwhile to synthesize different types of N-heteroacenes and study their structure–property relationships.²³ Li *et al.* synthesized linearly fused hexazapentacene derivatives with enhanced electron mobility.²⁴ Studies on pyrene fused N-heteroacenes have revealed promising potential for utilization in organic electronics and energy harvesting applications.²⁵ Hoffmann *et al.* investigated the influence of N atoms in the acene framework.²⁶ Das *et al.* synthesized an N-heteroacene and studied its hole mobility and acid-sensing properties.²³

Pyrazinoquinoxaline (PQ) derivatives are azaacenes, which have a central benzene ring symmetrically sandwiched between two pyrazine units. Their properties can be easily tuned by changing the substituent on the PQ.²⁷ The PQ unit can be considered as a good building block to synthesize low band gap organic semiconductors (OSCs) due to their planar π -conjugation and electron-deficient nature.^{28,29} Due to their symmetrically organized conjugated structure and multiple reactive sites, they provide an additional benefit for further structural

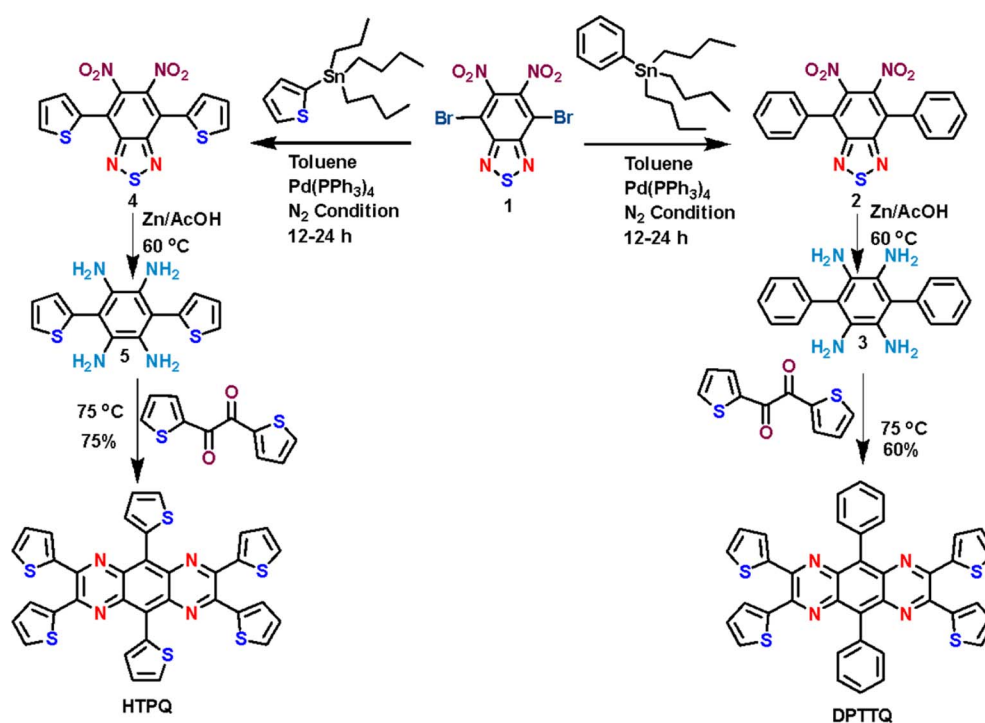
modification, and they may also be used to create luminescent materials.^{30,31} Structural modification can alter photophysical, mechanical, and electrochemical properties as well as change their band gap. Different PQ derivatives and their polymers with various substitutions have been studied for their photophysical properties, morphology, and performance in OFET, OLED, and OPV devices.^{27,32,33} Although many PQ derivatives have been reported to date, the mechanical properties of these molecules have remained relatively unexplored.

In this work, we present the synthesis, comprehensive characterization, mechanical property investigation, and device application of two recently developed novel PQ derivatives. Notably, these compounds demonstrate high solubility in common organic solvents and reasonable hole mobility in OFET devices. Moreover, the crystals of HTPQ showcase remarkable elastic flexibility, marking a notable milestone as the first documented instance of a PQ derivative exhibiting such elastic behaviour. This property is taken advantage of in the demonstration of a high-performance durable device with no degradation of device performance for up to 60 cycles of strain and projected retention for up to ~650 cycles of operation.

Results and discussion

Synthesis

The compounds 5,10-diphenyl-2,3,7,8-tetra(thiophen-2-yl)pyrazino[2,3-*g*]quinoxaline (DPTTQ) and 2,3,5,7,8,10-hexa(thiophen-2-yl)pyrazino[2,3-*g*]quinoxaline (HTPQ) have been synthesized by the condensation reaction of the corresponding tetraamino compounds with diketo compounds (Scheme 1). Compounds 3 and 5 were synthesized *in situ* from



Scheme 1 Synthesis of HTPQ and DPTTQ.



compounds **2** and **4** by reducing them with Zn/AcOH and H₂O. Compounds **2** and **4** were synthesized from **1** using a previously reported procedure (details in the ESI†).³⁴ The purity and formation of the compounds have been confirmed by ¹H, ¹³C NMR, HRMS, and single-crystal X-ray structures.

Optical and electrochemical properties

To get an idea about the optical properties of the molecules, the UV-vis spectra of DPTTQ and HTPQ were recorded using chloroform as a solvent (Fig. 1(a)). Both compounds show significant absorption in the visible spectral region. The absorption spectrum of DPTTQ shows two strong intensity peaks; the intense peak at 357 nm results from a π - π^* transition, while the significant peak at 486 nm results from intramolecular charge transfer.³⁵ Similarly, HTPQ has two strong intensity peaks at 399 nm and 518 nm. The optical bandgaps for DPTTQ and HTPQ were calculated using a Tauc plot and found to be 2.33 eV and 2.26 eV, respectively (Fig. 1(c) and (d)). The band gap decreases slightly once thiophene rings replace the phenyl rings. This phenomenon can be attributed to the stronger donor properties of thiophene relative to phenyl rings and the more planar conformation of HTPQ compared to DPTTQ. Fig. 1(b) depicts the emission spectra of DPTTQ and HTPQ. DPTTQ has an emission peak at 547 nm, while HTPQ has an emission peak at 708 nm. The fluorescence quantum yield for both compounds was calculated using eqn S(1).^{†36} The quantum yields (ϕ_f) for DPTTQ and HTPQ were determined to be 3.6% and 0.4%, respectively, with respect to quinine sulfate (quantum yield = 54%) in 0.1 M H₂SO₄ solution.³⁷

An electrochemical study of the compounds has been performed by recording cyclic voltammetry (CV) in CH₃CN : CH₂Cl₂ solution (1 : 6; v/v) containing compounds (2.0 mM) and tetrabutylammonium hexafluorophosphate (TBAPF₆, 0.1 M) as a supporting electrolyte at a scan rate of 50 mV s⁻¹. The onset oxidation potential ($E_{\text{ox}}^{\text{onset}}$) values of DPTTQ and HTPQ are 1.37 and 1.32 V_{Ag/AgCl}, whereas the onset reduction potential values ($E_{\text{red}}^{\text{onset}}$) are -0.90 and -0.83 V_{Ag/AgCl} (Fig. 2(a) and (b)). $E_{\text{ox}}^{\text{onset}}$ values were used to calculate HOMO energy levels (E_{HOMO}) by using eqn (1a), whereas LUMO energy levels (E_{LUMO}) were calculated from E_{HOMO} and E_{opt} (eqn (1b)). E_{HOMO} and E_{LUMO} for DPTTQ are -5.85 eV and -3.52 eV, whereas the corresponding values for HTPQ are -5.78 eV and -3.52 eV, respectively. The electrochemical band gaps are found to be 2.27 eV and 2.15 eV for DPTTQ and HTPQ, respectively, which closely match with the optical band gap value calculated from the Tauc plot.

$$E_{\text{HOMO}} = -[E_{\text{red}}^{\text{onset}} - E_{1/2(\text{ferro})} + 4.8] \text{ eV} \quad (1a)$$

$$E_{\text{LUMO}} = E_{\text{HOMO}} + E_{\text{opt}} \text{ eV} \quad (1b)$$

Electropolymerization of HTPQ was carried out using repetitive cycles (10) in an applied potential range from 0 to 1.1 V (Fig. 2(c)). The increase in both cathodic and anodic currents following each repetitive cycle demonstrated polymer formation on the surface of the electrode. (Fig. 2(d)) shows the scan rate dependence study of HTPQ at 50 mV s⁻¹ to 500 mV s⁻¹ with an interval of 50 mV s⁻¹. The linear increment of peak current with respect to the scan rate indicates that the polymer

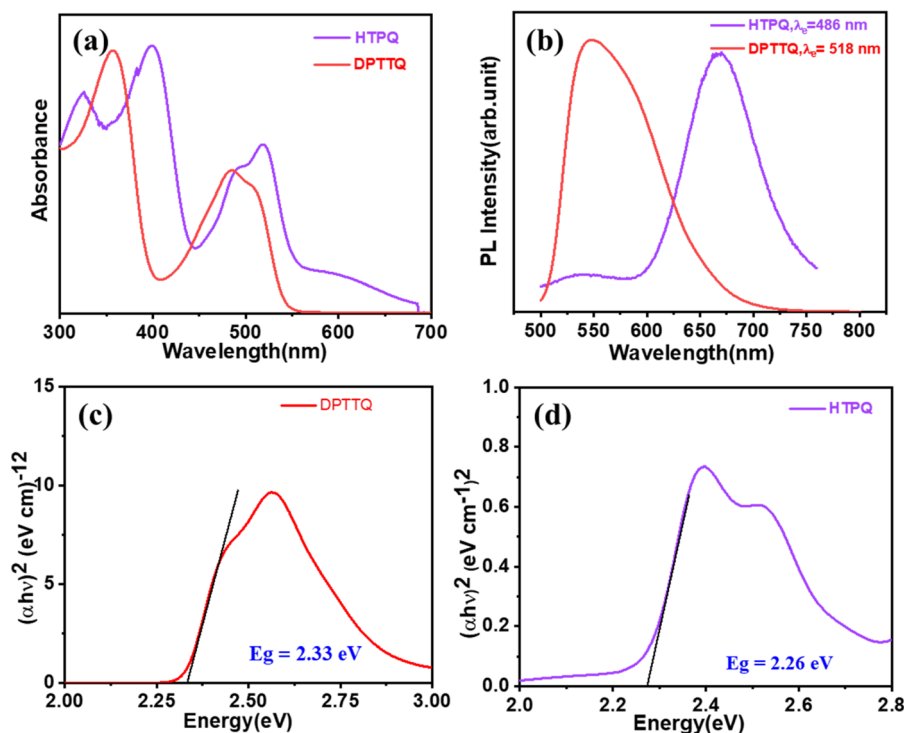


Fig. 1 (a) UV-visible spectrum of DPTTQ and HTPQ in chloroform, (b) PL spectrum, and Tauc plots to calculate the optical band gaps of (c) DPTTQ and (d) HTPQ.



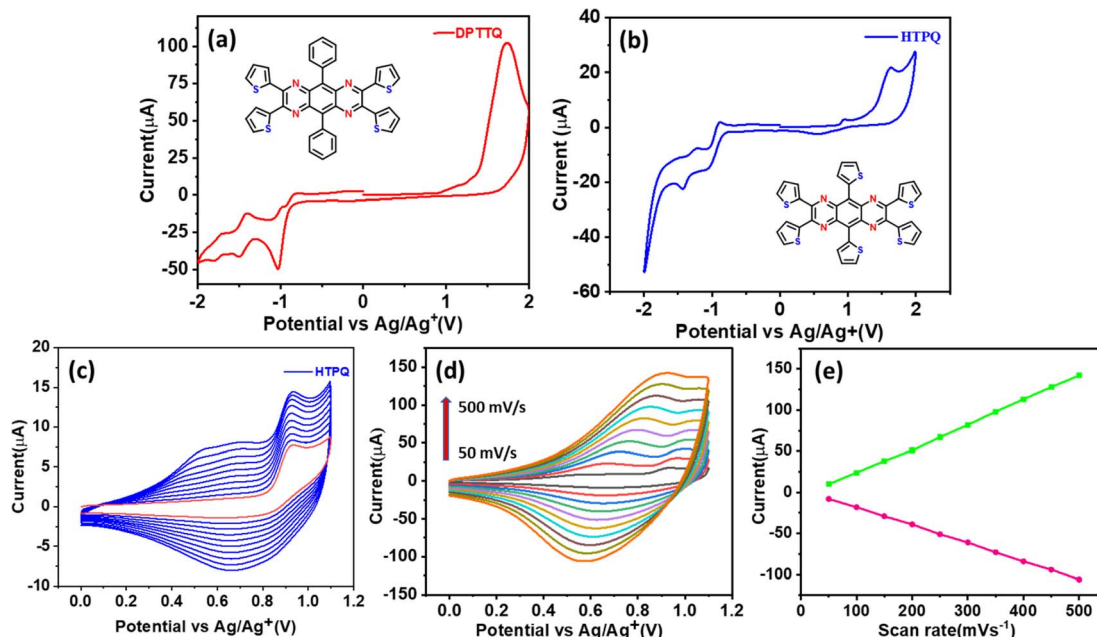


Fig. 2 (a) Cyclic voltammograms (CVs) of DPTTQ and (b) HTPQ, (c) CV with a repeated potential scan of HTPQ, (d) scan rate dependence study of pHTPQ films, and (e) linear fit of variation of current with the scan rate obtained from the figure (d).

films strongly attach to the electrode surface with a non-diffusional redox behavior³⁸ (Fig. 2(e)). DPTTQ could not be polymerized under electrochemical oxidative polymerization conditions. The DFT calculated HOMOs of DPTTQ and HTPQ showed significant coefficients only on 5,10-diphenyl/dithienyl substituents. In the case of DPTTQ, 5,10-substituents are phenyl groups that do not undergo electrochemical polymerization due to their weak donor properties. Due to a lack of significant HOMO coefficients, thienyl substituents at 2,3,7,8-positions may not be taking part in electrochemical polymerization.

X-ray single crystal analysis

The needle type single crystals of DPTTQ and HTPQ were obtained *via* the anti-solvent method from a dichloromethane solution with a hexane (anti-solvent) layer on top in 3–4 days (Fig. 5(a)). In the case of DPTTQ, a slightly higher diluted solution of dichloromethane gave thin and longer needles as compared to those obtained from concentrated solutions (thick needles). The solutions of DPTTQ and HTPQ in DCM were drop-cast over a polyethylene terephthalate (PET) substrate. We found that the crystal grown over the substrate (Form-B) is different from the crystals obtained by the slow evaporation technique (Form-A), in the case of DPTTQ, confirming the possibility of two polymorphs, which is evident from the PXRD, DSC, and Raman data (Fig. S5, S7, and S8†). To distinguish the two polymorphs (Form A and Form B) of DPTTQ, we performed a DSC analysis. Although their melting points are close, *i.e.*, 361 °C for Form A and 358 °C for Form B, there are notable differences in their phase transitions. Form A exhibits two phase transitions before melting, while Form B only shows one, occurring at a different temperature than Form A. Additionally, the recrystallization temperatures differ

significantly, with Form A at 268 °C and Form B at 228 °C, highlighting distinct crystal packing in the two polymorphs. The DSC data of HTPQ indicate that it melts at 371 °C. We have performed Raman spectroscopy of the thin films of Form A and Form B to check the possibility of an existing concomitant polymorph. However, our observations indicate that there is no possibility of concomitant polymorphs existing in these films. The Raman spectra of both polymorphs have significant differences. The Raman spectra recorded for different crystals of Form B are identical. Despite several attempts, it was not possible to grow single crystals suitable for structure determination by X-ray diffraction for the second polymorph (Form-B). In contrast, HTPQ crystals obtained *via* both slow evaporation and drop casting methods exhibit a needle-like shape. Consequently, the PXRD data of HTPQ crystals from drop casting match well with the simulated pattern generated using their single crystal data (Fig. S6(b)†). The crystal data of DPTTQ of Form-A reveal that it crystallizes in a monoclinic *C2/c* space group with a 2D ‘brick-layer’ arrangement, often referred to as a β -sheet packing motif (Fig. 4(a)).^{13,39} In the crystal structure, the aromatic core (pyrazinoquinoxaline ring or PQ core) is slightly distorted, while the peripheral phenyl rings are also significantly twisted with respect to the PQ core with a dihedral angle of about 44° (Fig. 3(a) and (b)). The distortion of the PQ core in DPTTQ may be caused by the high steric crowding of the phenyl rings.

HTPQ has a triclinic structure with a $P\bar{1}$ space group and exhibits a herringbone packing motif with dense face-to-face π -orbital overlap, often referred to as a γ -type structure^{13,39,40} (Figure 3(c) and 4(b)). The PQ core of HTPQ adopts a distorted structure with the thiophene rings A and B nearly in the same plane and another four thiophene units twisted out of the plane (Fig. 3(d)).



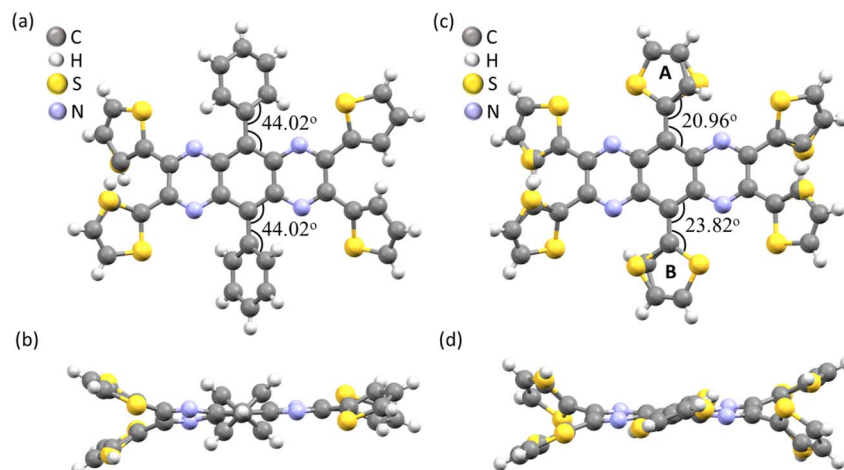


Fig. 3 Crystal structures of (a) DPTTQ and (c) HTPQ are represented with a ball-and-stick model. Side views of the molecules of (b) DPTTQ and (d) HTPQ.

It is generally known that in different crystal structures, the tighter the arrangement between neighbouring molecules, the better the charge transport due to stronger intermolecular interactions. In γ -type structures, the dense face-to-face π -orbital overlap primarily drives charge transport, which is expected to result in higher mobility compared to the β -sheet type packing motif.⁴¹ Analysing the crystal packing in the γ -type structure of HTPQ, it is evident that it possesses a corrugated packing pattern, which is also a key desirable condition for achieving elastic flexibility in crystals.^{42–44} Hence, the crystal packing of HTPQ aligns with the established favourable criterion for both higher mobility and elastic flexibility.

DFT calculations

To better understand the optoelectronic properties, we optimized the molecular structures of DPTTQ and HTPQ using B3LYP/6-311+G (d,p). The optimized structures obtained through DFT align with the structural features identified in the X-ray analysis of single crystals. The pyrazinoquinoxaline (PQ) core exhibits greater torsional twisting in DPTTQ, attributed to the presence of 5,10-diphenyl substituents, in contrast to HTPQ with 5,10-dithienyl substituents. The torsional angle between the PQ core and 5,10-diphenyl substituents is notably more significant in DPTTQ compared to the angle between the PQ core and 5,10-dithienyl substituents in HTPQ.

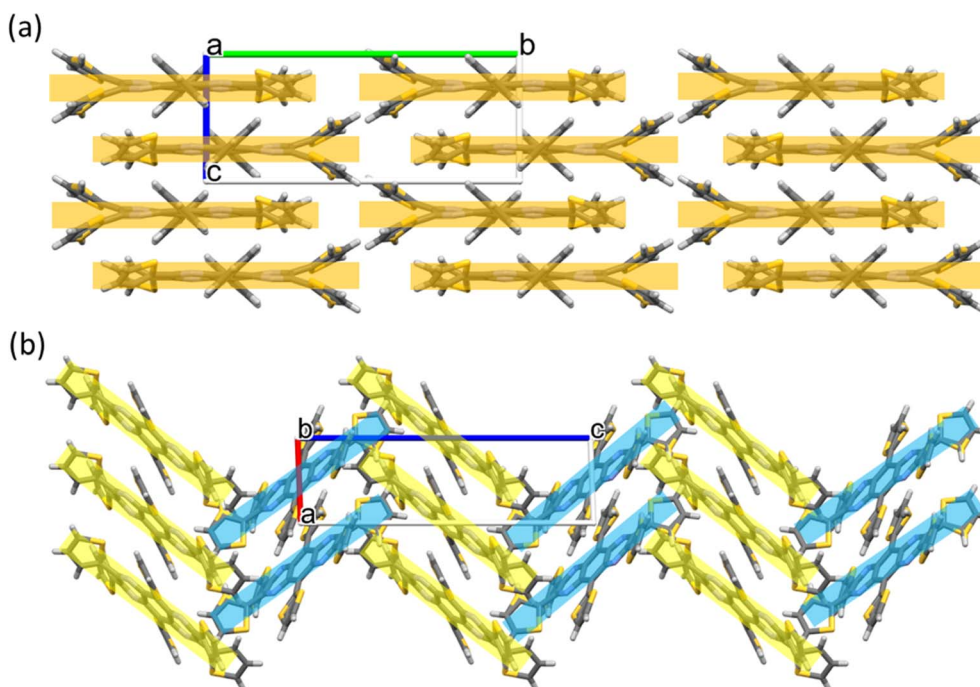
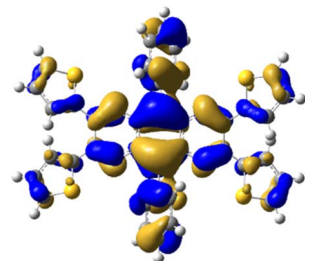
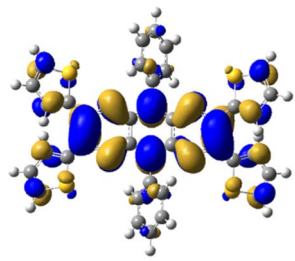
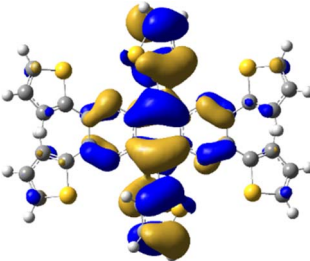
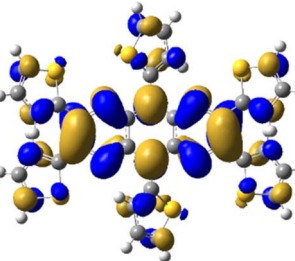


Fig. 4 Crystal packing of (a) DPTTQ with a β -sheet structure and (b) HTPQ with a γ -type structure in capped stick model.



Table 1 Frontier molecular orbitals of DPTTQ and HTPQ

Compound	HOMO	LUMO
DPTTQ		
HTPQ		

This structural variation is evident in the UV-vis absorption spectra, where HTPQ demonstrates absorption at longer wavelengths compared to DPTTQ. Time-dependent DFT (TD-DFT) calculations using B3LYP/6-31G(d) on the optimized structures reveal a longer wavelength and lower intensity HOMO–LUMO transition in HTPQ, as observed in the absorption spectrum centered at 600 nm (Fig. S10 and Table S2†). Conversely, in the case of DPTTQ, the HOMO–LUMO

absorption band occurs at a relatively lower wavelength and is integrated with the band centred at 486 nm (Fig. S9 and Tables S1† and 1).

Mechanical properties

Generally, the mechanical durability of functional materials can be improved by incorporating mechanical flexibility^{43,45} or self-

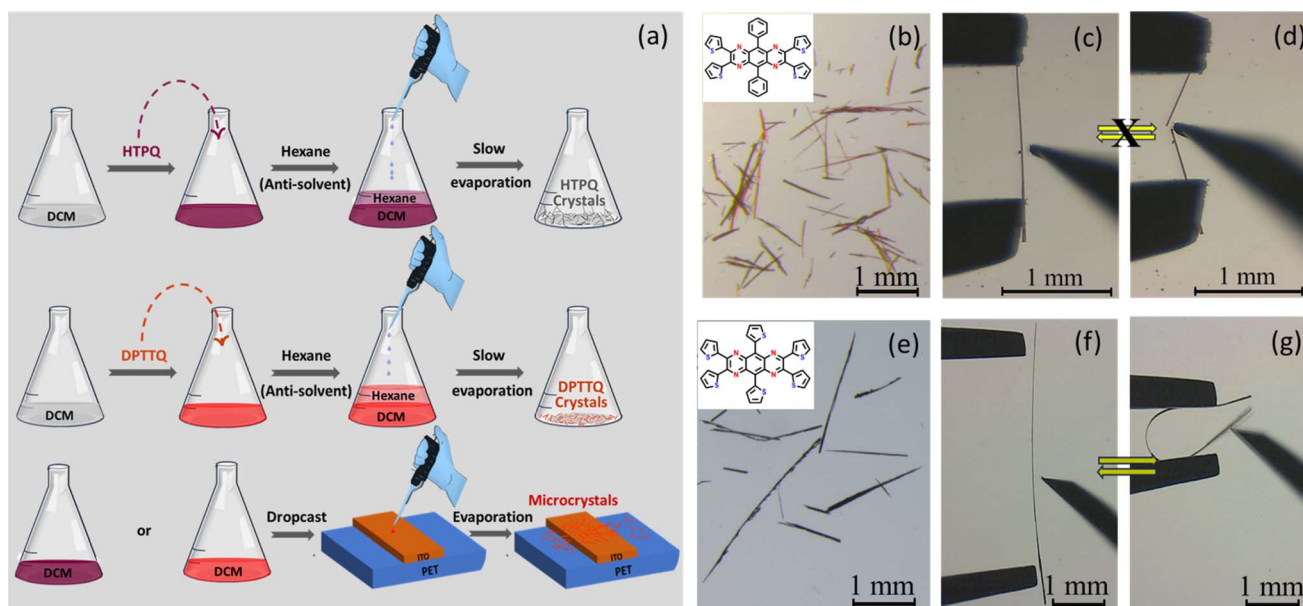


Fig. 5 (a) Schematic showing growth of DPTTQ and HTPQ crystals, (b) optical images of orange-colored crystals of DPTTQ, (c) and (d) video grabs, before and after the three-point bending mechanical tests of DPTTQ, (e) optical images of dark crystals of HTPQ, and (f) and (g) video grabs, before and during the three-point bending tests of HTPQ. Insets in (b) and (e) show the molecular structures of compounds DPTTQ and HTPQ, respectively.



healing nature^{46–48} and controlling the crystal packing in the materials. We explored the mechanical properties^{41,49–52} of the crystals of HTPQ and DPTTQ (Fig. 5). It was observed that HTPQ is elastically bendable (ESI Movie S1†),⁴³ whereas the latter is brittle under external mechanical stress (ESI Movie S2†).⁵³ To rationalize the distinct mechanical behaviour of the two crystals, we analysed their structures (Fig. 6, S11 and S13†). In the case of HTPQ, crystals grow along the [100] axis with two pairs of side faces (001)/(00-1) and (010)/(0-10). The major faces are (001)/(00-1) as identified from face indexing using a single crystal X-ray diffraction technique (Fig. S13(c)†). When a needle-shaped crystal is subjected to three-point bending tests by applying external mechanical stress with the help of forceps and a needle, it bends elastically on the major face and breaks when the stress is applied on the minor face, *i.e.* (010)/(0-10) face. In the crystal, the molecules are stacked along the crystal growth axis, *i.e.*, along the length of the crystal. Molecules in the adjacent stacked columns are tilted with respect to each other to form a corrugated structure with an angle of $\sim 102^\circ$ between the adjacent stacks.

Existing mechanisms suggest that corrugated stacks with buffering regions in crystal structures can accommodate elastic strain energy.^{42,44,54–56} During bending, the crystal's inner arc contracts, and the outer arc expands along the bending axis.

From SCXRD analysis of pristine crystals, it is evident that the packing in HTPQ adopts a corrugated packing dominated by dispersive interactions (Fig. 6). When the crystal is subjected to three-point bending, the angle between two molecules in the adjacent column (θ) is expected to decrease/increase on the outer/inner arcs of the crystal (see Fig. 6(c)). After the release of the stress, the molecules regain their original positions.

In contrast to HTPQ, DPTTQ crystals (Form A) are red-colored and grow along the [001] axis (Fig. S13(d)†). These crystals grow as both thin and slightly thick needles, depending on the crystallization conditions. In a three-point bending test, these crystals break easily from all the faces without showing any flexibility (Fig. 5(c) and (d)). DPTTQ molecules stack parallel to the length of the crystal. Here, we do not see corrugated layers; the molecules form parallel adjacent stacks (Fig. S11†). Perhaps, due to the lack of corrugated packing, the crystal is unable to accommodate elastic strain energy from any of the side faces and, hence, is brittle. The microcrystals of DPTTQ Form B also show brittle fractures under similar conditions (Fig. S12(b)†). As revealed by the mechanical bending tests on the crystals of HTPQ and DPTTQ, the former can bend smoothly into a loop and recover to their original shape without any permanent deformation upon releasing external mechanical stress, confirming their elastic nature. In contrast, crystals of

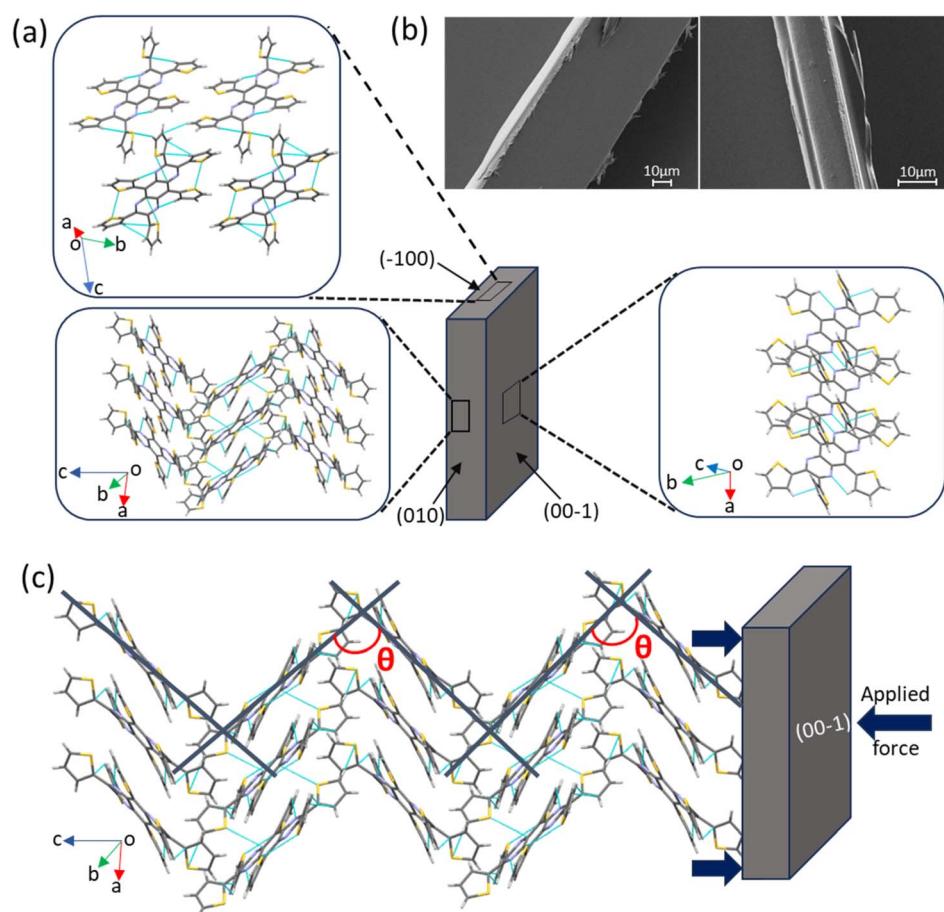


Fig. 6 (a) Structure of HTPQ crystals (interactions are shown with an edited CIF that does not contain disorder), (b) FESEM images of the major and minor faces of HTPQ crystals, and (c) schematic of the angle that is expected to change upon bending the crystal on the major face.



Table 2 Aspect ratio and elastic strain tolerance limit of the acicular single crystals of DPTTQ and HTPQ. Elastic strain tolerance limits are estimated from three-point flexural tests on each of the crystals

DPTTQ (brittle fracture)					HTPQ (elastic bending)				
Crystal no.	Length (mm)	Width (μm)	Aspect ratio (length/width)	Elastic strain (%)	Crystal no.	Length (mm)	Width (μm)	Aspect ratio (length/width)	Elastic strain (%)
1	0.5	13	38.5	0.9	1	1.1	26	42.3	3.5
2	0.4	10	40	0.6	2	3.3	71	46	3.6
3	0.7	16	43.8	0.73	3	1.4	26	53.8	4.2
4	0.6	13	46.2	0.4	4	0.7	12	58.3	3.11
5	0.4	8	50	0.5	5	1.2	17	70.6	3
6	0.8	15	52	0.86	6	1	13	77	3
7	0.9	16	56.3	0.6	7	4.3	50	86	3.9
8	0.9	13	69.2	0.93	8	3.3	34	97	3
9	0.5	6	83.33	0.82	9	2.5	25	100	4.1
10	1.1	13	84.61	0.83	10	3	30	100	3.1

DPTTQ Form A with comparable morphologies under similar conditions do not show a significant elastic nature.

Often, it is argued that thin needle-type crystals with a high aspect ratio (length x /width y) show higher elasticity than thick crystals. Hence, it becomes important to consider the aspect ratio, which is defined as the ratio between the length and width of crystals (x/y),⁵⁷ for comparing the mechanical properties of different forms or systems. We carried out a statistical analysis of the two crystals and plotted the aspect ratio against the elastic strain tolerance. When we compared the data from the DPTTQ and HTPQ crystals with comparable aspect ratios, the

elastic limit was found to be in the range of 0.4 to 0.9% and 3 to 4.2%, respectively (Table 2 and Fig. 7). This suggests that the DPTTQ crystals are inherently far less elastic than HTPQ crystals. Hence, the mechanical properties of the crystals studied here depend much more on their structure than on their morphology.

Flexible device study

To investigate the effect of mechanical strain on the electrical conductivity, we have utilized vertical sandwich devices of

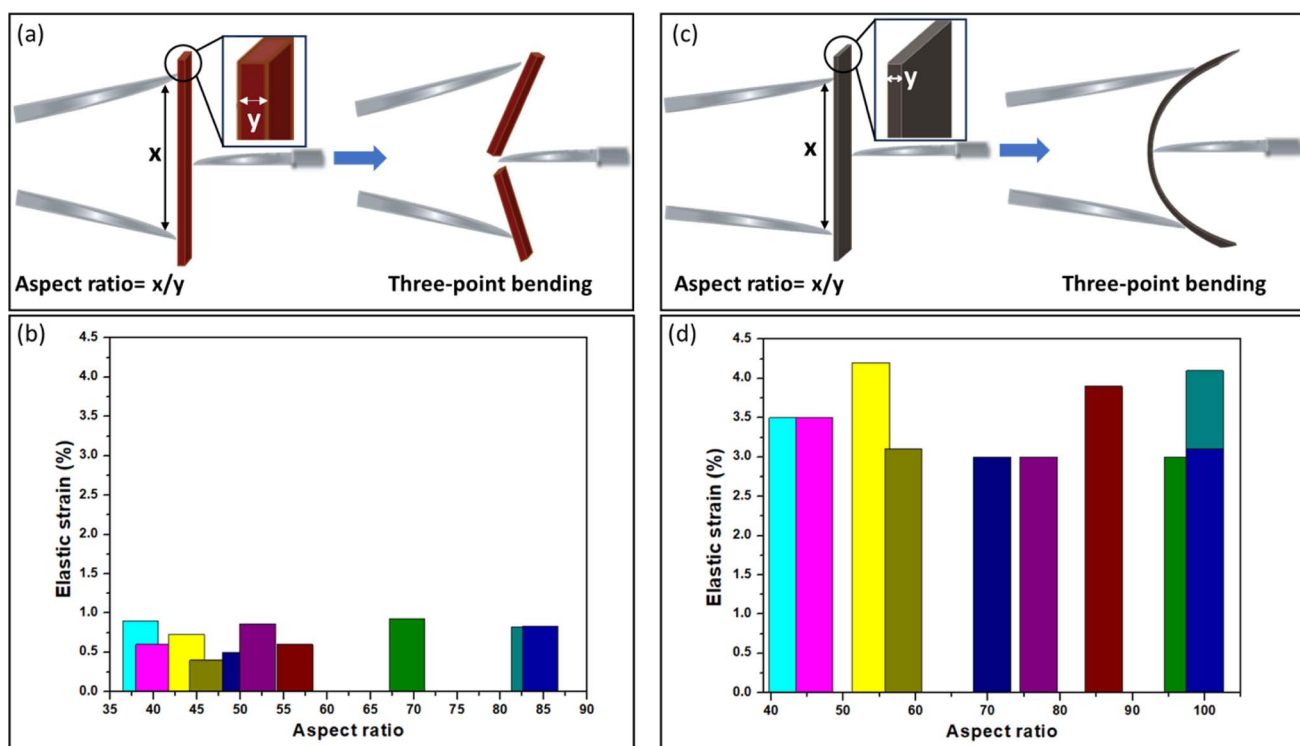


Fig. 7 (a) Schematic of brittle fracture of DPTTQ crystals and (b) histogram of elastic strain plotted against the aspect ratio of DPTTQ crystals (form-A) from the data set of Table 2. (c) Schematic showing elastic bending of HTPQ crystals and (d) histogram of elastic strain plotted against the aspect ratio for HTPQ crystals from the data set of Table 2.

DPTTQ and HTPQ fabricated on a flexible PET substrate (Fig. S18† depicts the fabrication process). I - V measurements were performed on these vertical devices and the device characteristics are presented in Fig. 8. In general, devices fabricated from HTPQ exhibit a current value of at least 3–4 times higher than those fabricated from DPTTQ. The conductivity of HTPQ-based devices was obtained to be $\sim(4.2 \pm 0.9) \times 10^{-8} \text{ S m}^{-1}$, which decreased to $\sim(2.3 \pm 0.7) \times 10^{-8} \text{ S m}^{-1}$ (Fig. S19†) for DPTTQ. We then subjected these flexible devices to significant mechanical strain by bending them with strain radii ranging from 15 mm to 2.5 mm (Fig. S20†), corresponding to a strain range of 0.43% to 2.6% (details of the strain calculation are in ESI Section 14). For flexible devices fabricated from DPTTQ Form B crystals, I_{max} (at 100 V) decreased by ~ 6 orders of magnitude as the strain increased from 0.43% (strain radius = 15 mm) to 1.3% (strain radius = 5 mm) (Fig. 8(a)), with the conductivity dropping to $(7.1 \pm 0.7) \times 10^{-14} \text{ S m}^{-1}$ (Fig. 8(c)). Interestingly, for the flexible devices fabricated with HTPQ crystals, we did not observe any degradation in the I_{max} value; instead, it increased (3–4 times the pristine value) as the strain radius was increased from 0.43% (strain radius = 15 mm) to 2.6% (strain radius = 2.5 mm) (Fig. 8(b)). The conductivity of the HTPQ-based flexible devices reaches a maximum value of $(1.6 \pm 0.1) \times 10^{-7} \text{ S m}^{-1}$ at 2.6% strain. The performance degradation in DPPTQ-based flexible devices is attributed to the brittle nature of the crystals, which cannot accommodate the strain, leading to crystals' breakdown and disrupted charge

transport. In contrast, devices fabricated from flexible crystals can accommodate the strain and retain the charge transport owing to the inherent flexibility of the semiconducting material. We then analysed the mechanical durability of the flexible devices by subjecting them to multiple cycles of strain with a 2.5 mm radius (2.6% strain). Consistent with the flexible nature of the crystals, no drop in conductivity was observed (Fig. 8(d)). Based on simple linear extrapolation, we expect that the devices will retain their conducting properties ($>10^{-10} \text{ S m}^{-1}$) for up to 650 cycles, which is significant considering the inherent crystalline nature of the material (Fig. S21†).

Bulk charge transport study

To obtain an understanding of the charge transport of these solution-grown crystals, we performed space charge limited current measurement by fabricating electron only and hole only devices from DPTTQ and HTPQ (device schematic in Fig. S22†). All the devices exhibited a distinct transition from a linear to an SCLC regime (Fig. 9(a)). The mobility was estimated from the SCLC regime using the Mott Gurney equation $J = \frac{9}{8} \epsilon_0 \epsilon_r \mu \frac{V^3}{L^3}$, where J is the current density, ϵ_0 is the vacuum permittivity, ϵ_r is the dielectric constant, V is the applied bias, and L is the thickness of the film. The hole mobility values (μ_h) for DPTTQ and HTPQ were obtained to be $2.1 \times 10^{-3} \text{ cm}^2 \text{ V}^{-1} \text{ s}^{-1}$ and $3.4 \times 10^{-3} \text{ cm}^2 \text{ V}^{-1} \text{ s}^{-1}$, respectively, and electron mobility (μ_e) values were found to be $5.7 \times 10^{-7} \text{ cm}^2 \text{ V}^{-1} \text{ s}^{-1}$ and $2.3 \times 10^{-4} \text{ cm}^2 \text{ V}^{-1}$

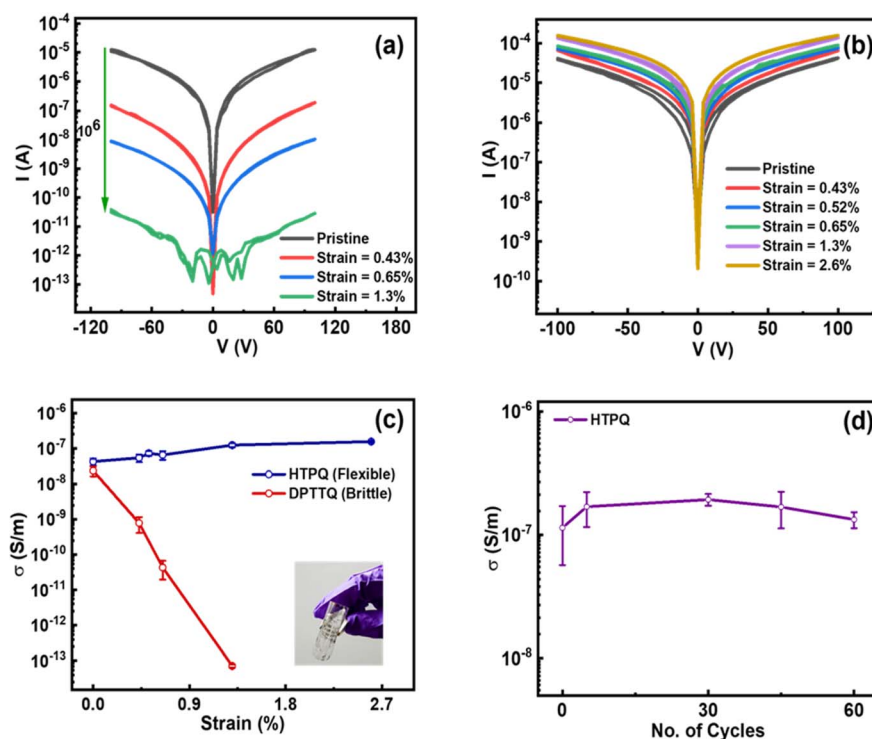


Fig. 8 I - V characteristics of flexible vertical devices fabricated from (a) DPTTQ and (b) HTPQ, upon bending with different extents of strain. (c) Variation in the conductivity of the flexible devices fabricated from DPTTQ (red) and HTPQ (blue) crystals as a function of strain (inset: an optical image of the flexible device). (d) Variation in the conductivity of the flexible devices fabricated from HTPQ crystals upon multiple cycles of bending at a strain radius of 2.5 mm. Error bars represent the standard deviation over 7 devices.



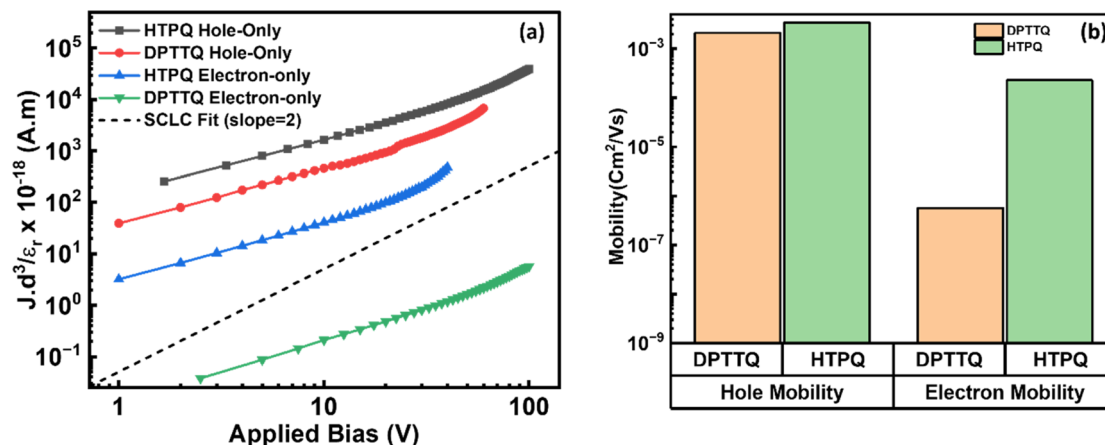


Fig. 9 Room temperature transport measurements. (a) J - V characteristics on the log-log scale for different molecules in electron-only and hole-only device configurations. The current density is scaled with the dielectric constant and film thickness to directly visualize the mobility trend. (b) Bar plot of the hole and electron mobility of both the molecules.

s^{-1} , respectively (Fig. 9(b)), indicating a general p-type nature of this semiconductor. However, the enhanced electron transport in HTPQ can possibly be attributed to the enhanced electron-donating nature of the thienyl substituents in HTPQ compared to the phenyl substituents in DPTTQ (evident from the electrochemical measurements). Moreover, it is evident from the relative energetics (Fig. S22†) that the hole only devices fabricated from the HTPQ based semiconductor exhibit a lower injection barrier in comparison to the hole only devices fabricated from DPTTQ, which can be correlated to the higher hole mobility. Notably, the near-ideal nature of the SCLC characteristics and relatively high bulk mobility indicate the advantages of these semiconducting materials for a variety of applications. To estimate the trap density of the molecules, we utilized the trap-filled voltage: $V_{\text{th}} = \frac{qn_t L^2}{2\epsilon}$ where q is the elementary charge of an electron, n_t is the trap density, L is the thickness of the semiconducting film, and ϵ is the permittivity of the thin film. The estimated trap densities were consistent with the trends of the observed mobility (Fig. S23†). Temperature dependent J - V characteristics were determined on all the devices. The charge transport exhibits a typical thermally activated behaviour (Fig. S24 and S25†) with the value of activation energy generally consistent with the trends of trap density estimated from the SCLC measurements at room temperature describing the internal consistency among the measurements.

In order to probe the inherent stability of the devices, we performed I - V measurements while the devices were continuously illuminated with a light source of intensity 200 W m^{-2} . Irrespective of continuous illumination, the devices exhibit outstanding stability to optical stress (Fig. S26†). Under ambient conditions, the devices also exhibit reasonable stability. DPTTQ devices exhibit only a marginal fall in conductivity from $6 \mu\text{S m}^{-1}$ to $\sim 4.8 \mu\text{S m}^{-1}$ over a period of 10 days, whereas HTPQ devices exhibit a decrease in conductivity from $\sim 22 \mu\text{S m}^{-1}$ to $\sim 5 \mu\text{S m}^{-1}$ (Fig. S27†), indicating the general stability of these semiconductors under ambient conditions.

Field effect transistor measurements

Finally, we fabricated a bottom-gate, bottom-contact field-effect transistor to obtain an understanding of the field effect charge transport of these semiconducting molecules. For the device fabrication, both DPTTQ and HTPQ were spin-coated on lithographically patterned substrates at 1000 rpm for 1 minute and annealed at 100°C for 30 minutes (device schematic in Fig. S28†). Transistor characteristics were measured inside a Lake-shore Probe station using a B1500A semiconductor characterization system. The devices exhibit a clean p-type output characteristic with a well-defined linear and saturation regime over the entire gate voltage range (Fig. 10(a) and (c)). However, these devices exhibit high threshold voltage (V_{th}) in the range of -10 V to -25 V , which is evident from the transfer characteristics shown in Fig. 10(b), (d) and S29.† This high value of V_{th} may be associated with the inherent doping of the semiconductor during the device fabrication process or the nature of traps at the dielectric semiconductor interface.^{3,58} The field-effect mobility for the best DPTTQ device in the saturation regime was obtained to be $0.0015 \text{ cm}^2 \text{ V}^{-1} \text{ s}^{-1}$ with an ON/OFF ratio $>10^3$ (Fig. 10(b)). In contrast, HTPQ devices exhibited a field-effect mobility that is at least one order of magnitude higher, reaching a value of $0.01 \text{ cm}^2 \text{ V}^{-1} \text{ s}^{-1}$ and an ON/OFF ratio of 10^4 (Fig. 10(d)).

In order to account for the high V_{th} values in the devices, we have quantified the reliability factor of mobility in these devices,⁵⁹ which was observed to be $>100\%$, indicating that the mobility values in the manuscript are rather conservative and underestimated (details in ESI Section 17). The higher hole mobility value in the case of HTPQ is likely due to the better crystal packing, which facilitates enhanced charge transport. Specifically, the smaller torsional angle between a thienyl ring and a PQ core than between a phenyl ring and a PQ core potentially makes the HTPQ structure more planar, thereby enhancing the in-plane field effect charge transport properties.^{60,61} Furthermore, thienyl acts as a stronger electron-donating substituent compared to phenyl. Therefore,



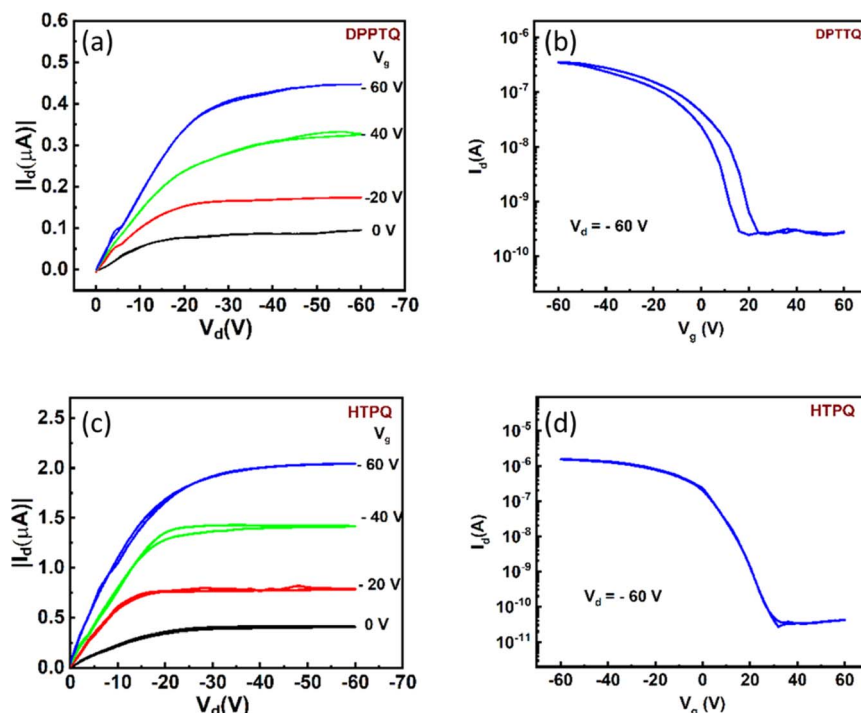


Fig. 10 (a) Output and (b) transfer characteristics measured on bottom contact bottom gate devices fabricated from the DPPTQ semiconductor. (c) Output and (d) transfer characteristics measured on bottom contact bottom gate devices fabricated from HTPQ semiconducting films.

thiophene transfers additional electrons to the PQ core of HTPQ, consequently enhancing the effective donor nature of the molecule, which results in higher p-type mobility in HTPQ.

The study emphasizes the close relationship between the mechanical and electronic properties of HTPQ and DPPTQ. Electronic properties, such as charge carrier mobility, are greatly affected by the molecular structure and how molecules are arranged in the solid state. When molecules are tightly packed, charge transport is usually improved due to a higher charge transfer integral, which may arise from a shorter π - π stacking distance or increased π -overlap. This molecular packing can also influence the material's mechanical flexibility. For example, molecules with corrugated packing often exhibit elastic behaviour, whereas those without such interactions are more prone to brittle fracture. In this study, HTPQ molecules show a corrugated crystal packing pattern with significant π - π interactions, leading to elastic behaviour and higher mobility compared to DPPTQ, which lacks these interactions.

Conclusion

In summary, we accomplished the synthesis of two pyrazinoquinoxaline (PQ) derivatives with thienyl and phenyl substitutions. Detailed structure–property correlation was obtained by investigating the optoelectronic properties, crystal packing, mechanical properties, and charge transport measurement of these PQ derivatives. Analysis of the HOMO and LUMO obtained from DFT calculations elucidates the facile electropolymerization of HTPQ and the inability of DPPTQ to undergo electropolymerization. The packing arrangement of

DPPTQ resembles a β -sheet structure, while HTPQ adopts a γ -type arrangement. Notably, HTPQ crystals display elasticity under bending stress, while both the polymorphic crystals of DPPTQ show brittleness. The charge transport behaviour indicates a clear p-type semiconducting nature. Owing to the difference in crystal packing, we observe a significant difference in the charge transport behaviour between HTPQ and DPPTQ. Devices fabricated from HTPQ exhibit a field effect transport of $0.01 \text{ cm}^2 \text{ V}^{-1} \text{ s}^{-1}$ and a bulk hole mobility of $3.4 \times 10^{-3} \text{ cm}^2 \text{ V}^{-1} \text{ s}^{-1}$. Moreover, flexible devices fabricated from HTPQ flexible crystals exhibit retention of performance for up to 650 cycles of operation, whereas DPPTQ crystal-based devices exhibit severe degradation of performance by five orders of magnitude with just one cycle of strain. Overall, our measurements underscore a clear correlation between chemical design and high-performance flexible devices, highlighting the advantages of the HTPQ molecule over DPPTQ.

Data availability

All data supporting the findings of this study including synthesis and characterization, single crystal analysis and mechanical properties, and device fabrication and characterization are presented in the ESI.†

Author contributions

J. B. and D. M. S. conducted the synthesis, characterization, and theoretical calculations. B. M., K. R. K., A. S., and A. N. performed the fabrication and characterization studies of the



devices. S. G. performed crystal structure analysis and conducted experiments on mechanical properties. All authors contributed to writing the manuscript. S. S. Z., C. M. R., and S. P. S. supervised the project.

Conflicts of interest

There are no conflicts to declare.

Acknowledgements

This work is financially supported by SERB, India, vide CRG/2023/004884. J. B. acknowledges the CSIR, India, for the Senior Research Fellowship (09/0921(12025)/2021-EMR-I). D. M. S. acknowledges the UGC, India, for the Senior Research Fellowship (16-6(DEC.2018)/2019(NET/CSIR)). S. G. acknowledges IISER Kolkata for the Junior Research Fellowship. The authors are thankful to the IISER Kolkata facilities. SPS acknowledges funding from the Royal Society London, through the Newton Alumni Fellowship and SERB Government of India for funding through SERB-SRG/2020/001641, and SERB-IPA/2021/000096 and DAE Government of India (RIN-4001). K. R. K., B. M., A. S., and A. N. acknowledge NISER for scholarships and facilities.

References

- 1 S. Allard, M. Forster, B. Souharce, H. Thiem and U. Scherf, *Angew. Chem., Int. Ed.*, 2008, **47**, 4070–4098.
- 2 A. L. Briseno, R. J. Tseng, M. M. Ling, E. H. L. Falcao, Y. Yang, F. Wudl and Z. Bao, *Adv. Mater.*, 2006, **18**, 2320–2324.
- 3 H. Sirringhaus, *Adv. Mater.*, 2014, **26**, 1319–1335.
- 4 G. Hong, X. Gan, C. Leonhardt, Z. Zhang, J. Seibert, J. M. Busch and S. Bräse, *Adv. Mater.*, 2021, **33**, 2005630.
- 5 J. D. Myers and J. Xue, *Polym. Rev.*, 2012, **52**, 1–37.
- 6 C. Liao and F. Yan, *Polym. Rev.*, 2013, **53**, 352–406.
- 7 T. Sekitani, T. Yokota, U. Zschieschang, H. Klauk, S. Bauer, K. Takeuchi, M. Takamiya, T. Sakurai and T. Someya, *Science*, 2009, **326**, 1516–1519.
- 8 C. Pitsalidis, A. M. Pappa, S. Hunter, M. M. Payne, J. E. Anthony, T. D. Anthopoulos and S. Logothetidis, *ACS Appl. Mater. Interfaces*, 2015, **7**, 6496–6504.
- 9 T. Someya, Y. Kato, T. Sekitani, S. Iba, Y. Noguchi, Y. Murase, H. Kawaguchi and T. Sakurai, *Proc. Natl. Acad. Sci. U. S. A.*, 2005, **102**, 12321–12325.
- 10 T. Sekitani, U. Zschieschang, H. Klauk and T. Someya, *Nat. Mater.*, 2010, **9**, 1015–1022.
- 11 L. Gao, *Small*, 2017, **13**, 1603994.
- 12 V. Raghuwanshi, D. Bharti and S. P. Tiwari, *Org. Electron.*, 2016, **31**, 177–182.
- 13 Y. Wang, L. Sun, C. Wang, F. Yang, X. Ren, X. Zhang, H. Dong and W. Hu, *Chem. Soc. Rev.*, 2019, **48**, 1492–1530.
- 14 K. Liu, B. Ouyang, X. Guo, Y. Guo and Y. Liu, *npj Flexible Electron.*, 2022, **6**, 1.
- 15 R. Samanta, S. Das, S. Mondal, T. Alkhidir, S. Mohamed, S. P. Senanayak and C. M. Reddy, *Chem. Sci.*, 2023, **14**, 1363–1371.
- 16 J. Li and Q. Zhang, *ACS Appl. Mater. Interfaces*, 2015, **7**, 28049–28062.
- 17 C. Gozálvez, J. L. Zafra, A. Saeki, M. Melle-Franco, J. Casado and A. Mateo-Alonso, *Chem. Sci.*, 2019, **10**, 2743–2749.
- 18 Y. Yamashita, *Sci. Technol. Adv. Mater.*, 2009, **10**, 024313.
- 19 W. Jiang, Y. Li and Z. Wang, *Chem. Soc. Rev.*, 2013, **42**, 6113.
- 20 U. H. F. Bunz and J. Freudenberg, *Acc. Chem. Res.*, 2019, **52**, 1575–1587.
- 21 J. E. Anthony, *Chem. Rev.*, 2006, **106**, 5028–5048.
- 22 A. Dreuw and P. Tegeder, *Phys. Chem. Chem. Phys.*, 2023, **25**, 17079–17091.
- 23 S. Das, A. Mandal, M. T. Alam, C. Kumar, A. Sarkar, S. P. Senanayak, S. Bhattacharyya and S. S. Zade, *ACS Appl. Mater. Interfaces*, 2022, **14**, 37982–37989.
- 24 G. Li, Y. Wu, J. Gao, C. Wang, J. Li, H. Zhang, Y. Zhao, Y. Zhao and Q. Zhang, *J. Am. Chem. Soc.*, 2012, **50**, 20298–20301.
- 25 B. L. Hu, C. An, M. Wagner, G. Ivanova, A. Ivanova and M. Baumgarten, *J. Am. Chem. Soc.*, 2019, **13**, 5130–5134.
- 26 M. Hoffmann, M. Ajdari, F. Landwehr, O. Tverskoy, U. H. F. Bunz, A. Dreuw and P. Tegeder, *Phys. Chem. Chem. Phys.*, 2022, **24**, 3924.
- 27 V. K. Vishwakarma, S. Nath, M. Gupta, D. K. Dubey, S. S. Swayamprabha, J. H. Jou, S. K. Pal and A. A. Sudhakar, *ACS Appl. Electron. Mater.*, 2019, **9**, 1959–1969.
- 28 L. P. Zhang, K. J. Jiang, G. Li, Q. Q. Zhang and L. M. Yang, *J. Mater. Chem. A*, 2014, **2**, 14852.
- 29 B.-L. Hu, K. Zhang, C. An, D. Schollmeyer, W. Pisula and M. Baumgarten, *Angew. Chem.*, 2018, **130**, 12555–12559.
- 30 L. P. Zhang, L. Kang, X. Li, S. Liu, T. Liu and Y. Zhao, *ACS Appl. Nano Mater.*, 2021, **2**, 2019–2029.
- 31 L. P. Zhang, X. Li, T. Liu, L. Kang, X. Huang and Y. Zhao, *Chem. Commun.*, 2020, **56**, 5544.
- 32 T. L. Dexter Tam, T. Salim, H. Li, F. Zhou, S. G. Mhaisalkar, H. Su, Y. M. Lam and A. C. Grimsdale, *J. Mater. Chem.*, 2012, **22**, 18528.
- 33 J. Quinn, C. Guo, L. Ko, B. Sun, Y. He and Y. Li, *RSC Adv.*, 2016, **6**, 22043–22051.
- 34 V. J. Bhanvadia, H. K. Machhi, S. S. Soni, S. S. Zade and A. L. Patel, *Polymer*, 2020, **211**, 123089.
- 35 S. Debnath, S. Chithiravel, S. Sharma, A. Bedi, K. Krishnamoorthy and S. S. Zade, *ACS Appl. Mater. Interfaces*, 2016, **28**, 18222–18230.
- 36 A. Chatterjee, A. K. Sharma, S. Pramanick, O. S. Jaykishan and P. Purkayastha, *J. Phys. Chem. C*, 2023, **127**, 797–806.
- 37 A. Chatterjee and P. Purkayastha, *Mater. Adv.*, 2021, **2**, 1343.
- 38 E. Sefer and F. Baycan Koyuncu, *Electrochim. Acta*, 2014, **143**, 106–113.
- 39 J. E. Campbell, J. Yang and G. M. Day, *J. Mater. Chem. C*, 2017, **5**, 7574–7584.
- 40 Jasmine Bezboruah CCDC 2254836: Experimental Crystal Structure Determination, 2023, DOI: [10.5517/ccdc.csd.cc2fpbn4](https://doi.org/10.5517/ccdc.csd.cc2fpbn4).
- 41 W. M. Awad, D. W. Davies, D. Kitagawa, J. Mahmoud Halabi, M. B. Al-Handawi, I. Tahir, F. Tong, G. Campillo-Alvarado, A. G. Shtukenberg, T. Alkhidir, Y. Hagiwara,



- M. Almehairbi, L. Lan, S. Hasebe, D. P. Karothu, S. Mohamed, H. Koshima, S. Kobatake, Y. Diao, R. Chandrasekar, H. Zhang, C. C. Sun, C. Bardeen, R. O. Al-Kaysi, B. Kahr and P. Naumov, *Chem. Soc. Rev.*, 2023, **52**, 3098–3169.
- 42 A. J. Thompson, A. I. Chamorro Oru , A. J. Nair, J. R. Price, J. McMurtrie and J. K. Clegg, *Chem. Soc. Rev.*, 2021, **50**, 11725–11740.
- 43 S. Ghosh and C. M. Reddy, *Angew. Chem., Int. Ed.*, 2012, **51**, 10319–10323.
- 44 S. Saha, M. K. Mishra, C. M. Reddy and G. R. Desiraju, *Acc. Chem. Res.*, 2018, **51**, 2957–2967.
- 45 B. Bhattacharya, A. A. L. Michalchuk, D. Silbernagl, N. Yasuda, T. Feiler, H. Sturm and F. Emmerling, *Chem. Sci.*, 2023, **14**, 3441–3450.
- 46 S. Bhunia, S. Chandel, S. K. Karan, S. Dey, A. Tiwari, S. Das, N. Kumar, R. Chowdhury, S. Mondal, I. Ghosh, A. Mondal, B. B. Khatua, N. Ghosh and C. M. Reddy, *Science*, 2021, **373**, 321–327.
- 47 S. Mondal, P. Tanari, S. Roy, S. Bhunia, R. Chowdhury, A. K. Pal, A. Datta, B. Pal and C. M. Reddy, *Nat. Commun.*, 2023, **14**, 6589.
- 48 P. Commins, M. B. Al-Handawi, D. P. Karothu, G. Raj and P. Naumov, *Chem. Sci.*, 2020, **11**, 2606–2613.
- 49 M. Almehairbi, V. C. Joshi, A. Irfan, Z. M. Saeed, T. Alkhidir, A. M. Abdelhaq, P. B. Managutti, B. Dhokale, T. Jadhav, C. Calvin Sun and S. Mohamed, *Chem.–Eur. J.*, 2024, **30**, e202400779.
- 50 P. Naumov, S. Chizhik, M. K. Panda, N. K. Nath and E. Boldyreva, *Chem. Rev.*, 2015, **115**, 12440–12490.
- 51 X. Yang, M. B. Al-Handawi, L. Li, P. Naumov and H. Zhang, *Chem. Sci.*, 2024, **15**, 2684–2696.
- 52 S. Mondal, C. M. Reddy and S. Saha, *Chem. Sci.*, 2024, **15**, 3578–3587.
- 53 C. M. Reddy, K. A. Padmanabhan and G. R. Desiraju, *Cryst. Growth Des.*, 2006, **6**, 2720–2731.
- 54 S. A. Rather and B. K. Saha, *CrystEngComm*, 2021, **23**, 5768–5773.
- 55 S. Hayashi, S. Yamamoto, D. Takeuchi, Y. Ie and K. Takagi, *Angew. Chem., Int. Ed.*, 2018, **57**, 17002–17008.
- 56 G. R. Krishna, R. Devarapalli, G. Lal and C. M. Reddy, *J. Am. Chem. Soc.*, 2016, **138**, 13561–13567.
- 57 A. Diez-Escudero, M. Espanol and M.-P. Ginebra, *Chem. Sci.*, 2024, **15**, 55–76.
- 58 H. Sirringhaus, *Adv. Mater.*, 2005, **17**, 2411–2425.
- 59 H. H. Choi, K. Cho, C. D. Frisbie, H. Sirringhaus and V. Podzorov, *Nat. Mater.*, 2018, **17**, 2–7.
- 60 M. Mas-Torrent, P. Hadley, S. T. Bromley, X. Ribas, J. Tarr s, M. Mas, E. Molins, J. Veciana and C. Rovira, *J. Am. Chem. Soc.*, 2004, **126**, 8546–8553.
- 61 S. P. Senanayak, A. Z. Ashar, C. Kanimozhi, S. Patil and K. S. Narayan, *Phys. Rev. B: Condens. Matter Mater. Phys.*, 2015, **91**, 115302.

